The Performance of Sensitivity-Maps Method in Reconstructing Low Contrast and Multi-Contrast Objects for Microwave Imaging Applications

https://doi.org/10.3991/ijoe.v19i08.38665

Basari[1,2(✉)], Syahrul Ramdani[1]
[1]Biomedical Engineering, Department of Electrical Engineering, Faculty of Engineering, Universitas Indonesia, West Java, Indonesia
[2]Research Center for Biomedical Engineering, Faculty of Engineering, Universitas Indonesia, West Java, Indonesia
basyarie@eng.ui.ac.id

Abstract—The microwave imaging system for breast tumor/cancer detection requires high sensitivity to detect abnormal tissue that has little contrast in high-density breasts. This paper proposes a qualitative microwave imaging system simulation based on inverse scattering using the sensitivity-maps method. This method utilizes two measurement types for system calibration: a reference object as a scatterer-free background and a calibration object to obtain the system's impulse response. The object under test (OUT) consists of an object with low dielectric contrast and a phantom with multiple low dielectric contrasts (multi-contrast). Reconstruction is carried out on three types of S-parameter measurement data, namely S_{11}, S_{21}, and a combination of both. S-parameters are measured at several frequencies, which are 3, 10, 14, 15, 16, 20 GHz, and the combination of all those frequencies (multifrequency). Reconstructed images show that the system is capable of reconstructing dielectric objects accurately. Quantitatively, the results show that the multifrequency S_{21} measurement yields the best image quality with relative root mean squared error (RRMSE) values of 0.1272 and structural similarity index (SSIM) of 0.9076. The designed imaging system also successfully reconstructs multi-contrast phantom accurately with RRMSE of 0.1434 and SSIM of 0.4609.

Keywords—image reconstruction, inverse scattering, microwave imaging, multifrequency imaging, sensitivity-maps

1 Introduction

Microwave imaging has been widely applied in various fields. Several fields are of interest to researchers around the world, such as the military for detecting (remote sensing) [1], security for revealing hidden weapons [2], and medical imaging for diagnosing tumor/breast cancer [3]. Breast cancer is one of the most common causes of death for women worldwide. Early detection of breast cancer is necessary to get early treatment and increase survival chances. Microwave imaging could potentially become

a complementary modality to the current golden standard modalities for the early detection of breast cancer. Electromagnetic waves offer low-cost and low-risk advantages due to their relatively inexpensive components and non-ionizing waves. However, microwave imaging for the detection of breast cancer requires high sensitivity to detect abnormal tissue at an early stage. High sensitivity is required because the dielectric property of abnormal breast tissue has a small contrast compared to normal tissue in high-density breasts [4], [5]. Furthermore, there are challenges in the application of microwave imaging for medical purposes, such as penetration depth, resolution limit, tissue heterogeneity, etc. [6]

In general, there are two image reconstruction methods in microwave imaging, namely quantitative and qualitative [7]. In quantitative reconstruction, the reconstructed image is the approximate value of the actual dielectric property as a function of the position [8]. In contrast, qualitative reconstruction only provides information on the magnitude's distribution of the dielectric property, so it can only detect the position and estimate the shape as well as the size of objects with contrasting dielectric properties relative to the surrounding object background [9]. Quantitative imaging focuses on an iterative algorithm to solve the inverse problem accurately, so the reconstruction process is often sensitive and time-consuming. Qualitative imaging does not aim to find the exact dielectric value but instead detects the position and shape of the abnormal object by using a simpler technique to reduce computation time.

Several qualitative reconstruction methods commonly used include microwave holographic imaging [10]–[12], confocal imaging [13]–[15], and time-reversal imaging [16]–[18]. These three methods can reconstruct the image in a relatively fast time. However, these commonly used methods have low sensitivity to detect small contrast differences and objects with a lot of contrast (multi-contrast). This paper aims to evaluate the performance of the sensitivity method [19], [20] in reconstructing low contrast and multi-contrast object qualitatively using the sensitivity method. This method considers the scattering effect by using an incident field signal as a reference object and a calibration object as a sensitivity parameter to calibrate the system. This method also offers an easy reconstruction process because the inversion process is carried out directly on the spatial domain, so the calculations are relatively simple and fast.

The reconstructed images are analyzed both qualitatively and quantitatively using the relative root mean squared error (RRMSE) and structural similarity index (SSIM) parameters. Analysis is carried out on variation of S-parameter measurements and measurement frequency to evaluate the performance of the sensitivity-maps algorithm. In addition, a phantom consisting of three objects with different permittivity contrasts and shapes is also reconstructed to test the imaging system's ability to detect multi-contrast objects.

2 Sensitivity-maps method

Qualitative imaging using the sensitivity-maps method was first proposed in [19], [20]. This method uses the S-parameter response in the frequency domain as data for image reconstruction and utilizes special objects that serve as a calibration on the imaging system. The S-parameter measurement of the calibration object acts as a sensitivity

parameter that shows the S-parameter changes in the background medium when there is a contrast that scatters the field. The reconstruction algorithm in this method is based on the Fréchet derivative of the residual data, which can be seen in Equation (1), where $\Delta R_i^{(m)} \left| \varepsilon(r') \right| = R_i^{(m)} \left| \varepsilon(r') \right| - \bar{R}_i^{(m)}$ and i is the antenna position index.

$$D^{(m)}(r_n') = \sum_{i=1}^{N_R} \left\{ \Delta R_i^{(m)} \cdot \left(\frac{dR_i^{(m)}}{d\varepsilon_n'} \right)^* \right\} \tag{1}$$

The reconstructed $D^{(m)}$ is a function of position (r_n') on the nth voxel. This function is known as complex jacobian maps/sensitivity-maps/power maps. This function describes the intensity of the scattering at that position. The component $\left(\frac{dR_i^{(m)}}{d\varepsilon_n'} \right)^*$ is the S-parameter sensitivity or the change in response of the background medium when disturbed in the form of different permittivity contrasts. This S-parameter sensitivity serves as a system calibration on the sensitivity-maps method.

In this method, the S-parameter sensitivity is obtained by measuring three types of objects, namely the reference object (RO), the calibration object (CO), and the object under test (OUT). RO is an object that is used as a baseline for measurement. This value is obtained by measuring the S-parameter when there is no scatterer object on the background medium. S_{RO} shows the S-parameter magnitude as the incident field of the antenna. CO is an RO inserted with a calibration object with a very small electrical size. S_{CO} acts as a sensitivity parameter that shows the change in S-parameter when RO (normal condition) is scattered by the calibration object. OUT represents the object of interest that is going to be reconstructed. S_{OUT} shows the total S-parameter measurement results of the object being tested. This parameter represents the total field of the antenna. Illustrations of the three types of object measurements can be seen in Figure 1.

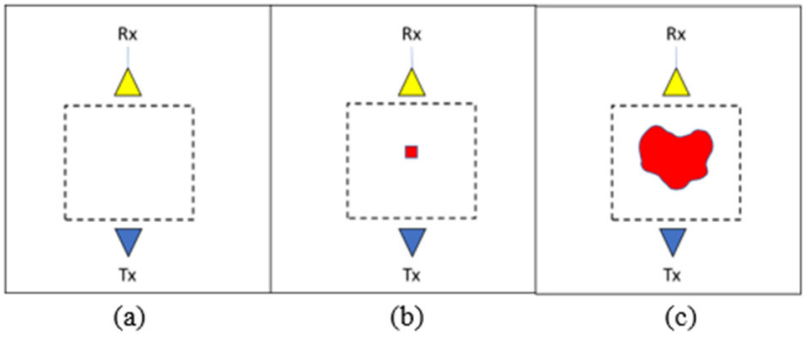

Fig. 1. Illustration of three types of object measurements: (a) reference object (RO), (b) calibration object (CO), and (c) object under test (OUT)

In terms of S-parameter, equation (1) can be rewritten into equation (2) [21], where $\zeta = 1,2,\ldots, N_T$, is the index of type S-parameter measurement (S_{11}, S_{21}, etc.), r' is the index of reconstructed pixels, and r_i, $i = 1,2,\ldots, N_R$ is the position of the antenna during

the i-th measurement. $\Delta S^{(m)}_{OUT(\zeta)}$ is the scattering part of the S_{OUT} which is obtained by subtracting the S_{RO} from S_{OUT} as in Equation (3) [21]. The amount of measurement performed for one frequency m is $N_T \times N_R$.

$$D^{(m)}(r') = \sum_{\zeta=1}^{N_T}\sum_{i=1}^{Ns} \Delta \boldsymbol{S}^{(m)}_{OUT(\zeta)}(r_i) \cdot \left[\frac{dS^{(m)}_{RO(\zeta)}(r_i)}{d\varepsilon(r')}\right]^* \tag{2}$$

$$\Delta \boldsymbol{S}_{OUT} = \boldsymbol{S}_{OUT} - \boldsymbol{S}_{RO} \tag{3}$$

The S-parameter sensitivity $\left[\frac{dS^{(m)}_{RO(\zeta)}(r_i)}{d\varepsilon(r')}\right]^*$ is derived into Equation (4) where ΔS_{CO} is the scattering part of S_{CO} that can be calculated with Equation (5). Substituting Equation (4) to Equation (2) and then normalizing it in respect to RO permittivity $\delta\varepsilon_{RO}$, the final reconstruction equation can be written as Equation (6).

$$\left[\frac{dS^{(m)}_{RO(\zeta)}(r_i)}{d\varepsilon(r')}\right] = \frac{\Delta S^{(m)}_{CO(\zeta)}(r_i, r')}{\delta\varepsilon_r(CO)} \tag{4}$$

$$\Delta \boldsymbol{S}_{CO} = \boldsymbol{S}_{CO} - \boldsymbol{S}_{RO} \tag{5}$$

$$M^{(m)}(r') = \sum_{\zeta=1}^{N_T}\sum_{i=1}^{Ns} \Delta S^{(m)}_{OUT(\zeta)}(r_i).\left[\Delta S^{(m)}_{CO(\zeta)}(r_i, r')\right]^* \tag{6}$$

3 Simulation Setup

3.1 Data acquisition configuration and measurement frequency

A pair of antennas consisting of a transmitter and receiver is used to measure the S-parameter as data to be reconstructed into an image. These antennas are positioned to face each other with a certain distance between them, where the object under test is placed in the middle. The data acquisition pattern used is a planar raster scan in which the Tx-Rx antennas pair are simultaneously translated in the x-axis direction with a certain step distance until they reach the end of the imaging area. Next, the antennas pair will move in the y-axis direction with the same step and repeat the scanning process in the x-axis direction. The receiving antenna measures the S-parameter at each translational position until covering the entire imaging area. The data acquisition configuration used for all objects is illustrated in Figure 2.

In microwave imaging, measurement frequency is an important parameter that must be considered. The scattering characteristic of microwave depends on the ratio of the wavelength to the scatterer object's electrical size. Object with a much smaller size than the measurement wavelength will make the wave penetrates through the object without

any scattering and will not be detected by the receiving antenna. On the other hand, a much larger object will cause most of the incident wave to be reflected hence less effective for the data acquisition configuration used. Ultrawideband (UWB) antenna has been widely used due to its multifrequency capabilities [22]–[24]. Various wavelengths will provide various spatial information to produce an image with good detail and contrast.

In this paper, the object scanned is designed to have a small size, with the longest dimension being 10 mm, to imitate abnormal tissue in the breast. Therefore, several measurement frequencies are sampled to determine the effect of wavelength on object size. The measurement frequency range is 3–20 GHz, where it is then sampled into 3 GHz, 10 GHz, 14 GHz, 15 GHz, 16 GHz, and 20 GHz to find the optimal single frequency. Based on the Nyquist rate theorem, the sampling frequency used must be at least twice or greater than the highest frequency of the signal to be reconstructed to obtain perfect reconstruction results [25]. Therefore, the translation step Δr_i as the spatial sampling was chosen at 10 mm where 16 GHz is chosen as the highest frequency to test under sampling conditions at 20 GHz. The design of the antennas and all test objects, as well as the data acquisition, are simulated on computer simulation technology (CST) microwave studio software.

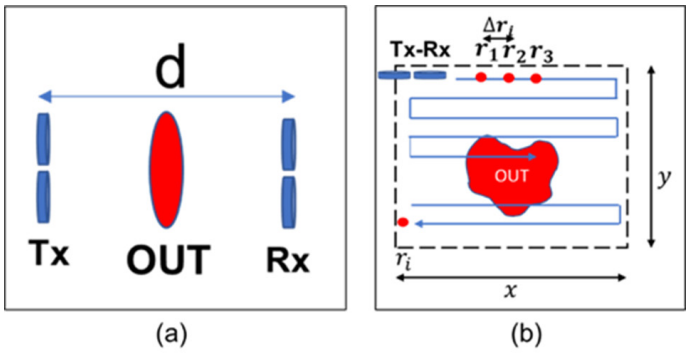

Fig. 2. Data acquisition configuration for all objects: (a) top view and (b) front view

3.2 Dipole antenna design

A pair of dipole antennas are chosen as data acquisition sensors, where one antenna acts as a transmitter and another as the receiver. Although the dipole antenna has a large beamwidth for imaging applications, this type of antenna is simple to design and takes significantly less time to simulate the scanning process. The dipole's length L, gap width G, and radius R can be changed to obtain the desired resonant frequency [26]. The final dimension of the dipole antenna for each frequency are shown in Table 1. Each antenna has S_{11} below –30 dB for each working frequency, indicating the antenna could radiate the power with insignificant return loss.

Table 1. The final dimension of dipole antenna for each measurement frequency

Frequency (GHz)	Dimension (mm)		
	Length (L)	Gap Width (G)	Radius (R)
3	47.15	0.2383	0.01
10	14.062	0.07	0.02
14	10.068	0.05	0.01
15	9.41	0.036	0.01
16	8.8108	0.04	0.01
20	7.028	0.035	0.01

3.3 Reference object (RO) design

A reference object (RO) is an object with a known relative permittivity as a reference when no scatterer object is in it. The reference object used is air as the background medium with a relative permittivity of $\varepsilon_b = 1 + 0j$. The reference object's permittivity value acts as the background in the image. In practice, the S-parameter measurement of the RO must be carried out according to the data acquisition configuration. However, the RO measurement in this setup is carried out in a simulation where no noise due to external interference is present. Therefore, measurement in all positions will give the same S-parameter result, so it is sufficient to measure once for each frequency when the two antennas are arranged to face each other and separated by a certain distance. The distance between the transmitting and receiving antennas is d = 5 cm. This is decided based on the far-field region of the lowest frequency of 3 GHz. The configuration of the RO measurement simulation can be seen in Figure 3. The S-Parameters measured are S_{11} and S_{21}.

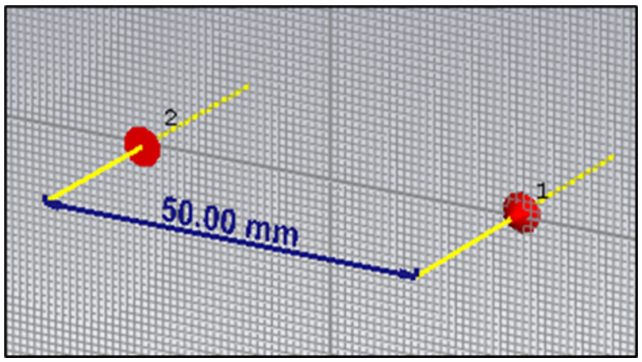

Fig. 3. Configuration of S_{RO} measurement simulation

3.4 Calibration object (CO) design

The Calibration Object (CO) is an RO with a small object inserted as a scatterer. The S-parameter of CO (S_{CO}) measurement aims to observe the change in S_{RO} when there is another object with known permittivity contrast scatters the incident field. The scatterer on the calibration object can be designed as a cube or a ball of a small size.

A scatterer object used is a cube with a similar size as the sampling step and the pixel size, which is $1 \times 1 \times 1$ cm^3. The relative permittivity of the object is $\Delta\varepsilon_{CO} = 1.1 + 0\,j$, so the permittivity contrast to the air background is 0.1. The configuration of the simulated CO measurement is shown in Figure 4. The sensitivity-maps reconstruction algorithm requires full S_{CO} measurements to be performed on a small scatterer object when placed on each voxel of the imaging. In the case of our configuration, the resulting image has a size of 21×21 pixels hence there are 441 measurements for one position of the CO cube, and 194,481 measurements are required to obtain the entire S_{CO} set. The requirement is very time-consuming and impractical in either simulation or direct measurement.

Fortunately, the background medium/RO of the imaging system can be assumed to be homogeneous over all (x,y) coordinates, so the number of S_{CO} measurements can be drastically reduced. The measurement of S_{CO} is possible to be carried out once for each frequency when the scatterer object is in the center of the imaging area. S_{CO} for the other scatterer 'objects' position can be obtained by translating the coordinates of the initial center CO measurements. The coordinate translation is performed by utilizing the shift property of the two-dimensional Fourier transform. This technique is known as the 2D Fourier shift.

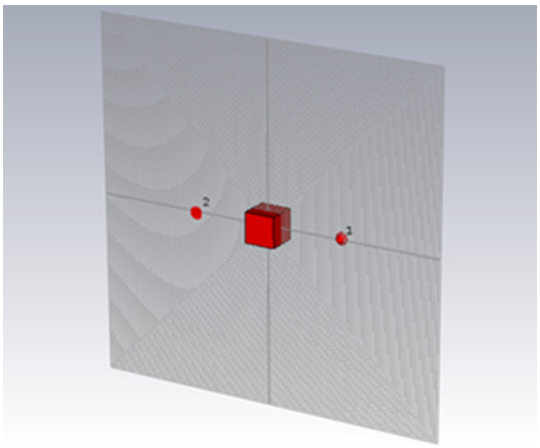

Fig. 4. Configuration of S_{CO} measurement simulation

3.5 Object under test (OUT) design

Two types of objects are designed as an object under test (OUT). Those objects are F-shaped dielectric with homogenous permittivity and phantom with three different permittivity. The F-shaped dielectric object and its dimension can be seen in Figure 5a. This object has a relative permittivity of $\varepsilon_{rOBJ} = 1.2 + 0j$, so the permittivity contrast to the air background is 0.2. In addition, a phantom is designed as an OUT to assess the sensitivity of the imaging system in reconstructing multi-contrast objects. The phantom has an elliptical base shape to mimic the shape of the breast. Next, additional square and rectangular objects are inserted into the elliptical object to represent abnormal and other normal tissue. Phantom design and configuration are shown in Figure 5b and Table 2.

Table 2. Multi-contrast phantom design configuration

Objects	Parameter	Value
Background–Air	X	20 cm
	Y	20 cm
	ε_b	1 + 0j
Object 1–Ellipse	d_x	7 cm
	d_y	9 cm
	ε_1	1.1 + 0j
Object 2–Square	$l_x = l_y$	2 cm
	ε_2	1.2 + 0j
Object 3–Rectangular	g_x	5 cm
	g_y	1 cm
	ε_3	1.3 + 0j

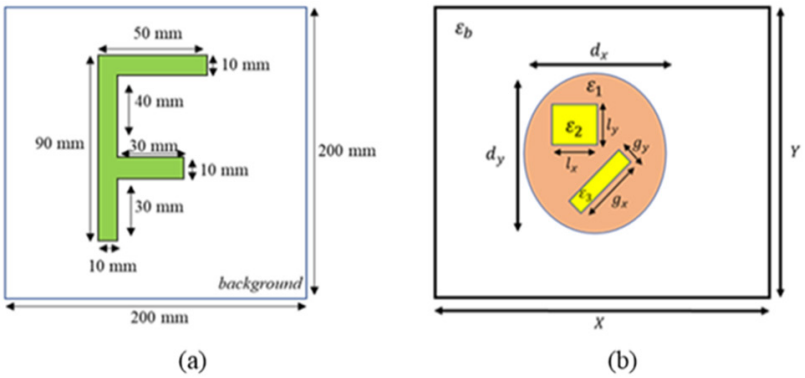

Fig. 5. Design of object under test (OUT): (a) F-shaped object and (b) multi-contrast phantom

4 Results

Image reconstruction is performed using MATLAB software. Numerical phantom is created for the reference image. Their pixel size is adjusted to have identical shape with reconstructed image. Qualitative analysis is conducted to evaluate the reconstructed images by comparing the image's shape, size, and position to the actual object. Meanwhile, quantitative parameters relative root mean squared error (RRMSE) and structural similarity index (SSIM) are used to assess further the effect of variations in S-parameter measurement type and frequency on the quality of reconstructed images. These parameters are calculated by comparing reconstructed image to reference numerical phantom images.

4.1 Reconstructed images of F-shaped object

Reconstructed images of F-shaped OUT for S-parameter measurement types S_{11}, S_{21} both combined are shown in Figures 6, 7, and 8, respectively. Figure 6 shows the reconstructed images of S_{11} measurement from the F-shaped object at each frequency. The reconstructed images do not provide accurate information on the permittivity contrast of objects at a frequency below 20 GHz. At a frequency of 20 GHz, the reconstructed image has shown the appropriate shape, size, and position but the permittivity contrast distribution is still uneven in the letter "F".

Figure 7 shows the reconstructed images of S_{21} measurement from F-shaped object at each frequency. At a frequency of 3 GHz, the reconstructed image still does not provide accurate information. At a frequency of 10 GHz, the reconstructed image has started to show the shape of the letter "F", but the size of the object does not match, and it still resembles a scattering. The reconstructed image from a frequency of 14 GHz gives a quite clear result, but the contrast distribution is also not evenly distributed. The images from frequencies of 15 and 16 GHz give the best visual results where the shape, size, and position of the object are accurate, as well as even permittivity distribution. The reconstructed image at 20 GHz provides good contrast, but additional shapes are detected in the background that can be mistaken as other objects. This can be caused by under-sampling conditions because the measurement translation step does not meet the Nyquist criteria at that frequency.

Figure 8 shows the reconstructed images by summing both S_{OUT} data at each frequency. At frequencies of 3, 10, and 14 GHz, the summation makes the reconstructed image qualitatively worse due to the long line in the S_{11} data. Meanwhile at frequencies of 15, 16, and 20 GHz, the reconstructed images do not change significantly and only change the contrast ratio between the object and the background.

Figure 9 shows the reconstructed images of the multifrequency measurement from three types of data. Reconstructed image of S_{11} data does not show the 'object's shape. The reconstructed S_{21} data have the best quality qualitatively. The image shows the shape of the object with accurate size, position, good contrast with the background, and an even distribution of permittivity. The results of multifrequency reconstruction for the combined data also successfully show the shape of an object with accurate size and position but with different contrast. The addition of S_{11} makes vertical lines appear in the background that resembles artifacts.

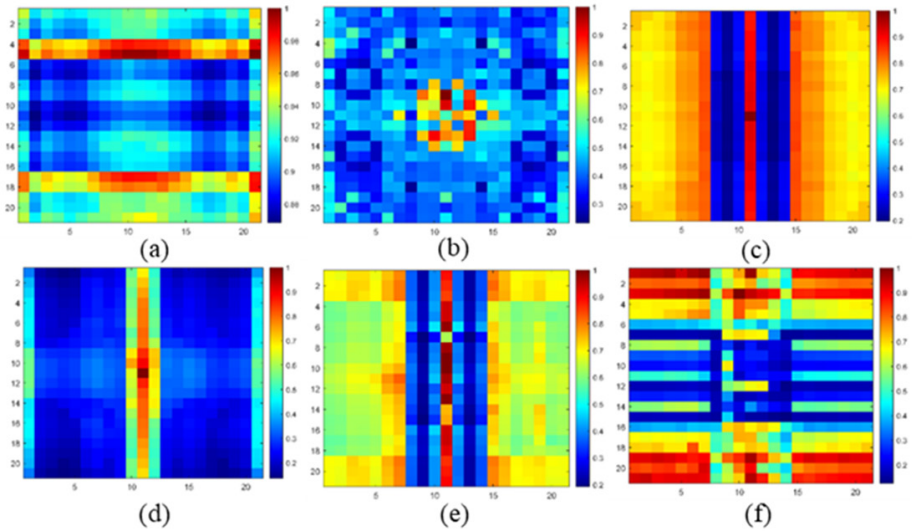

Fig. 6. Reconstructed images of F-shaped dielectric from S_{11} measurements at frequencies: (a) 3 GHz, (b) 10 GHz, (c) 14 GHz, (d) 15 GHz, (e) 16 GHz, (f) 20 GHz

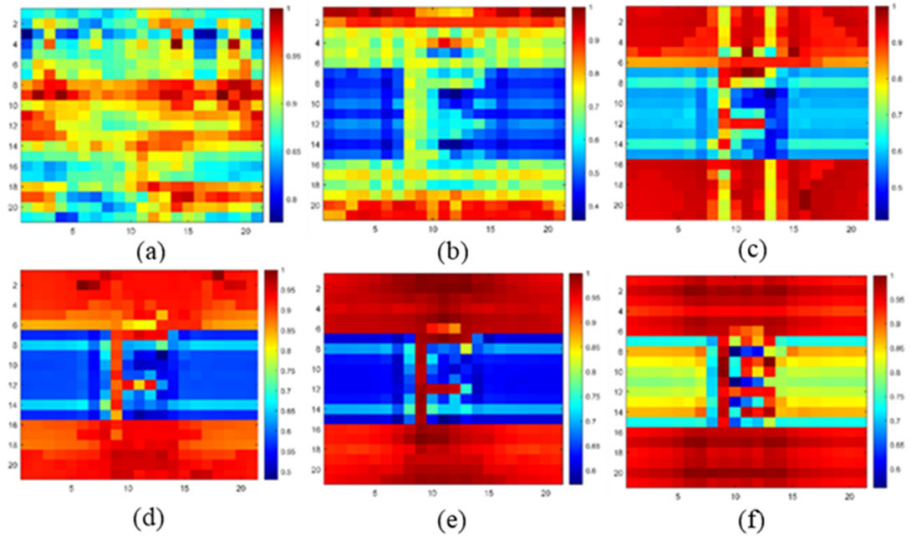

Fig. 7. Reconstructed images of F-shaped dielectric from S_{21} measurements at frequencies: (a) 3 GHz, (b) 10 GHz, (c) 14 GHz, (d) 15 GHz, (e) 16 GHz, (f) 20 GHz

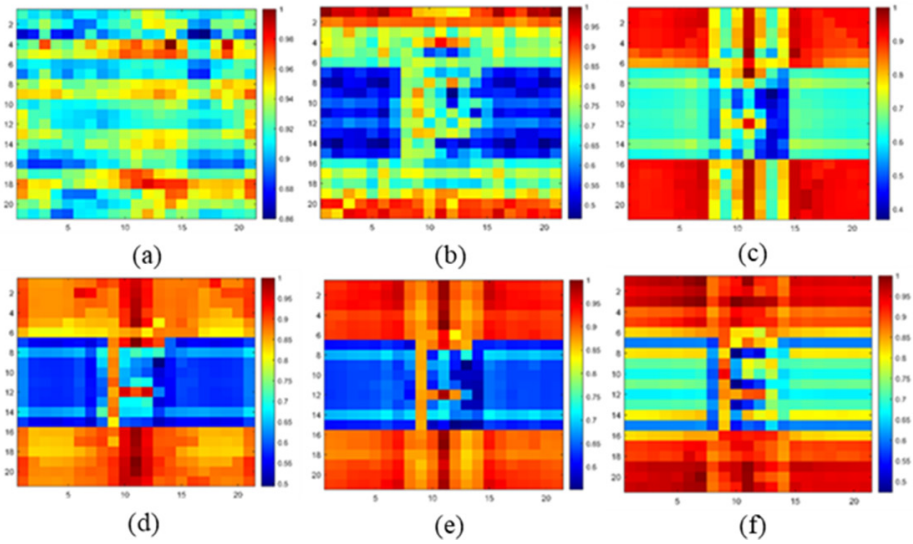

Fig. 8. Reconstructed images of F-shaped dielectric from combined S-parameter measurements at frequencies: (a) 3 GHz, (b) 10 GHz, (c) 14 GHz, (d) 15 GHz, (e) 16 GHz, (f) 20 GHz

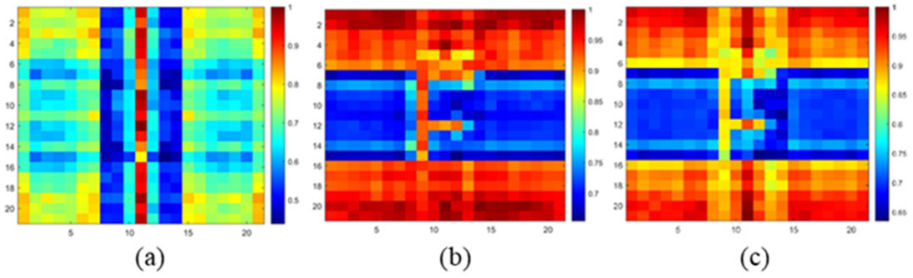

Fig. 9. Reconstructed images of F-shaped dielectric from reconstructed images for multifrequency measurement types: (a) S_{11}, (b) S_{21}, and (c) combined S_{OUT}

4.2 Image analysis of reconstructed F-shaped object

The RRMSE and SSIM calculation results for all types of S-Parameter measurements at each frequency are listed in Table 3, and a graph of the comparison of the S-Parameter types and the frequency of measurements to the RRMSE and SSIM of the reconstructed image is shown in Figure 10. RRMSE calculation shows that S_{11} reconstructed images have much higher RRMSE than the other two types of data. This indicates that S_{11} images have the largest error in pixel intensity. This result supports the visual qualitative analysis where it does not represent the object accurately except at the frequency of 20 GHz. The S_{21} and combined S-parameters reconstructed images have RRMSE differences that are not too significant where the two results alternately

have the lowest value in the frequency range used. Overall S_{21} gives the smallest average RRMSE for each frequency compared to other types of S-parameter measurements.

Table 3. RRMSE and SSIM of reconstructed F-shaped images

Frequency (GHz)	RRMSE			SSIM		
	S_{11}	S_{21}	Combined	S_{11}	S_{21}	Combined
3	0.096	0.1177	0.1134	0.1107	–0.1649	–0.0206
10	0.3639	0.3622	0.2439	–0.2055	0.3912	0.1934
14	0.661	0.2801	0.3325	–0.0555	0.6122	0.4972
15	0.4589	0.2586	0.2149	–0.173	0.7251	0.7637
16	0.6069	0.1729	0.2063	–0.1116	0.7418	0.7992
20	0.6696	0.1504	0.2226	0.3849	0.4834	0.6094
Multi-frequency	0.3391	0.1272	0.1473	–0.1117	0.9076	0.8854

If we look at the RRMSE results for each frequency, the 3 GHz frequency gives the lowest RRMSE value. This shows that the object's pixel intensity and background contrast have a small error compared to the reference image even though visually, the object is not detected at all at that frequency. Apart from the 3 GHz frequency, the 15 GHz frequency produces images with the smallest RRMSE average compared to other frequencies. Overall, RRMSE does not give constant linear results for each frequency. However, combining frequency lowers the RRMSE value, and multifrequency images have the smallest average RRMSE compared to -frequency that successfully detects objects.

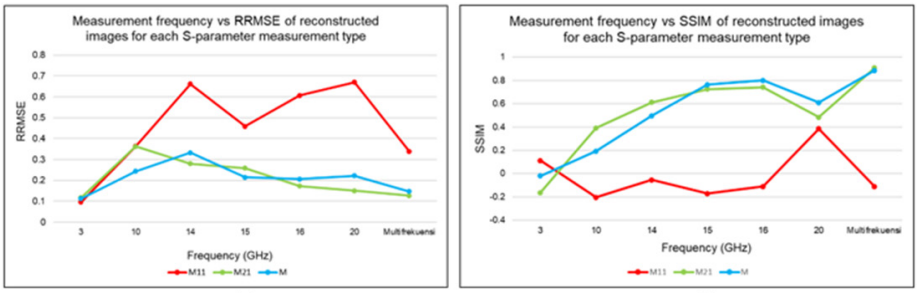

Fig. 10. Comparison of S-parameter types and measurement frequency to: (a) RRMSE of reconstructed image, (b) SSIM of the reconstructed image

Based on the SSIM calculation, the result of S_{11} reconstructed images have the lowest SSIM for each frequency compared to the other two types of data. These results show the lowest structural similarity compared to the reference image. This is also in accordance with the visual qualitative analysis. Just like the RRMSE parameter, the S_{21} and combined S-parameter reconstructed images did not show a significant difference

in SSIM. The two types alternately show the highest SSIM in the measurement frequency range used. Overall, the reconstructed image with combined data has the highest average SSIM with a small margin to S_{21}.

Analyzing at each frequency, S_{11} reconstructed image does not give a conclusive result. This can be seen in the negative SSIM value at five frequency points out of seven measurement frequencies, which again supports the qualitative analysis. Meanwhile, both S_{21} and combined S-parameter show an increase in the value of SSIM along with the increase in frequency, although then SSIM decreases again at a frequency of 20 GHz. This decrease occurs due to other contrasts detected in the image caused by under-sampling at that frequency where the spatial sampling used is already far below the Nyquist criteria. The difference in the highest SSIM values between 10 and 14 GHz frequencies with 15 and 16 GHz frequencies indicates that at 10 and 14 GHz frequencies, S_{11} data does not contribute to improving image quality. However, at the frequency of 15 and 16 GHz, S_{11} data contributes so that it increases the SSIM value.

From the entire single frequency range, the reconstructed image at a frequency of 16 GHz produces the highest SSIM value. Overall, the result of multifrequency reconstruction of S_{21} have the highest SSIM value with a margin that is not too large from the combined multifrequency data. However, the results of multifrequency reconstruction of the combined data have the highest SSIM average. All image reconstruction results show that the designed imaging system has accurately reconstructed dielectric objects with small contrast.

4.3 Reconstructed images of multi-contrast phantom

The result of F-shaped reconstructed images indicates that a frequency of 16 GHz offers optimal results in terms of qualitative and quantitative. Therefore, the simulation of S-parameter measurements of the phantom is carried out at a frequency of 16 GHz. The reconstructed image of multi-contrast phantom for each type of measurement data is shown in Figure 11. Based on the reconstructed images, the S_{11} data is still not able to provide information on the shape of the object like the previous F-shaped object. The S_{21} reconstructed image successfully detects all the contrast in the phantom. The white line as a reference can be seen in Figure 11b. Quantitative analysis is also carried out by calculating the RRMSE and SSIM of the reconstructed images. The result of the RRMSE and SSIM calculation from the reconstructed images for each image are listed in Table 4.

The calculation of quantitative parameters shows that the S_{11} reconstructed image has the worst quality, with the highest RRMSE value and the lowest SSIM. This is in accordance with the qualitative analysis where the phantom could not be detected on the S_{11} measurement. Quantitative parameters show an increase in the quality from S_{21} and combined S-parameter reconstructed images. Overall, the result of the combined S-parameter has the best RRMSE and SSIM. The SSIM value obtained is lower than the previous F-shaped object reconstruction result. This can be caused by the lack of measured spatial sampling, resulting in poor spatial resolution. In addition, errors in modelling the phantom reference image also play a role in producing low SSIM values.

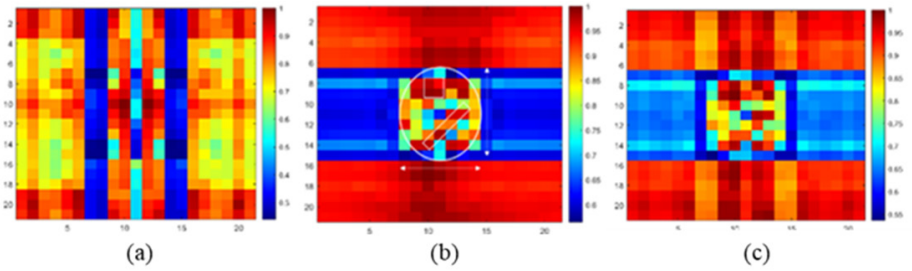

Fig. 11. Reconstructed images of multi-contrast phantom for measurement types: (a) S_{11}, (b) S_{21}, and (c) combined S_{OUT}

Table 4. RRMSE and SSIM of reconstructed multi-contrast images

S-Parameter Type	RRMSE	SSIM
S_{11}	0.4152	0.1405
S_{21}	0.1507	0.391
Combined	0.1434	0.4609

5 Discussion

Two objects with different permittivity contrast are reconstructed using the sensitivity method to evaluate its performance. The results are compared qualitatively and quantitatively with the reference numerical phantom image. This study uses both S_{11} and S_{21} parameter simulation data for image reconstruction as well as combination of both. The simulation is conducted in the sampled frequency of 3 – 16 GHz which theoretically will capture more information of the image.

The result shows that S_{11} parameter data overall does not seem to give any meaningful information for the reconstructed images. This is because S_{11} represents the reflected field back to the transmitter antenna. Meanwhile, S_{21} gives the most contribution to the shape of the object as it is the ratio between received field to transmitted field. However, quantitative parameter calculation shows that combination of both S_{11} and S_{21} parameter gives better reconstructed image which means both parameters carry information to the overall object. From the frequency standpoint, the higher frequency gives better spatial resolution and quantitative parameter. This agrees theoretically with the spatial resolution of microwave imaging which is approximately $\frac{\lambda_b}{4}$ [21]. The highest frequency 20 GHz has a wavelength of 14.99 mm which corresponds to spatial resolution of 3.74 mm. The lower frequency 10 GHz gives poorer spatial resolution which can be seen by its inability to reconstruct the width of the object accurately. The lowest frequency 3 GHz does not even show any actual shape as its wavelength is too big compared to object size so it will just pass through as if it sees nothing. However, like the S-parameter, combining every frequency will give a better reconstructed image because each frequency carries information which will contribute to overall image. Hence, we can improve the spatial resolution even more by using antenna with a higher bandwidth.

The proposed sensitivity-maps method successfully reconstructed both F-shaped phantom with low permittivity and multi-contrast phantom accurately. The reconstruction time is very fast because it's calculated directly in spatial domain. The stripe-like shape in the background is considered as artefact because it is undesired from the reconstructed image and gives non-uniformity background as well as apodization. This mainly appears because the dipole antenna used in this simulation has an omnidirectional radiation pattern, which will give a very wide beam in vertical direction as shown in the middle of the image. This should be removed by using another antenna with more directional radiation in the future. Another consideration is the modelling error within the simulation software which unfortunately cannot be eliminated.

Qualitative imaging is more widely used in the medicine field. The proposed sensitivity-maps is one of qualitative imaging which can reconstruct images faster than previously developed CT-based image reconstruction systems because it reconstructs directly in spatial domain instead of on frequency domain like CT-based one. The sensitivity-maps method also successfully detected a more complicated object with multiple permittivity contrast where this is still difficult to achieve with CT-based methods. This study also shows better spatial resolution due to higher frequency and broader frequency, as well as complex object with multiple contrast, and faster reconstruction compared to other popular qualitative microwave imaging technique mentioned before such as microwave holographic imaging [10]–[12] and confocal imaging [13]–[15]. Table 5 shows comparison between sensitivity-maps method and previous methods as well as other popular qualitative method.

Table 5. Comparison to previous and other methods

Methods	Frequency	Object	Author
CT-based (fbp and art)	3 GHz	Simple cube or cylinder with one contrast	2016–2019. Basari, et al [27]–[30]
Holographic	1.5–1.9 GHz	Cylinder with one contrast	2021. H. Wu, et al [10]
	1–4 GHz	Only numerical	2019. L. Wang, et al [11]
Confocal Imaging	0.8–2.2 GHz	Sphere with one contrast	2015. L. Guo & A. M. Abbosh [13]
	3–5 GHz	Sphere with one contrast	2017. W. Shao, et al [14]
	1.5–4.5 GHz	Sphere with one contrast	2020. S. A. S. Karamfard & B. M. Asl [15]
Sensitivity-maps	3, 14–20 GHz	F-shaped and multi-contrast phantom	This study

6 Conclusions

The simulation of a microwave imaging system based on the inverse scattering sensitivity-maps method has succeeded in reconstructing a dielectric object in the shape of the letter "F" with permittivity contrast into a qualitative image. Qualitatively and quantitatively, the S_{11} measurement simulation produces the worst quality image,

while the S_{21} measurement simulation produces the best quality image with the lowest RRMSE value of 0.1272 and the highest SSIM of 0.9076. An increase in the frequency of a single measurement will improve the quality of the reconstructed image qualitatively and quantitatively to a certain point where the measurement is under-sampling. The reconstructed image on a single frequency of 16 GHz has the best quality, with the lowest RRMSE value of 0.1729 and the highest SSIM of 0.7992.

Combining all single measurement frequencies (multifrequency) improves the quality of the reconstructed image qualitatively and quantitatively. The resulting image has the best overall quality, with an RRMSE value of 0.1272 and an SSIM of 0.9076. The designed imaging simulation system has successfully reconstructed a phantom consisting of three objects with different permittivity contrasts into a qualitative image. The resulting image is qualitatively accurate and has the lowest RRMSE value of 0.1434 and the highest SSIM of 0. 4609.The results show that the sensitivity-maps method has high sensitivity to reconstruct dielectric objects with small dielectric contrast or objects with multi-contrast.

7 Acknowledgement

The research was partly supported by PUTI Pascasarjana 2022 Grant No. NKB-308/UN2.RST/HKP.05.00/2022 from Universitas Indonesia.

8 References

[1] K. Lewis, "Challenges in military remote sensing," *Electro-Optical Remote Sensing, Detect. Photonic Technol. their Appl.*, vol. 6739, p. 67390J, 2007. https://doi.org/10.1117/12.753508

[2] W. Tan, P. Huang, Z. Huang, Y. Qi, and W. Wang, "Three-dimensional microwave imaging for concealed weapon detection using range stacking technique," *Int. J. Antennas Propag.*, vol. 2017, 2017. https://doi.org/10.1155/2017/1480623

[3] M. Pastorino, "Electromagnetic imaging: Methods and applications," *Mediterr. Microw. Symp.*, vol. 2015-January, pp. 2–5, 2015. https://doi.org/10.1109/MMS.2015.7375427

[4] M. O'Halloran, D. Byrne, R. C. Conceição, E. Jones, and M. Glavin, "*Anatomy and Dielectric Properties of the Breast and Breast Cancer*," 2016. https://doi.org/10.1007/978-3-319-27866-7_2

[5] A. Martellosio et al., "Dielectric properties characterization from 0.5 to 50 GHz of breast cancer tissues," *IEEE Trans. Microw. Theory Tech.*, vol. 65, no. 3, 2017. https://doi.org/10.1109/TMTT.2016.2631162

[6] A. Vander Vorst, A. Rosen, and Y. Kotsuka, "*RF/Microwave Interaction with Biological Tissues*," 2006. https://doi.org/10.1002/0471752053

[7] R. Chandra, H. Zhou, I. Balasingham, and R. M. Narayanan, "On the Opportunities and Challenges in Microwave Medical Sensing and Imaging," in *IEEE Transactions on Biomedical Engineering*, vol. 62, no. 7, pp. 1667–1682, 2015. https://doi.org/10.1109/TBME.2015.2432137

[8] L E. Larsen and J. H. Jacobi, "*Medical Application of Microwave Imaging*". New York: IEEE Microwave Theory and Techniques Society, 1995.

[9] R. A. Williams and M. S. Beck, "*Process Tomography: Principles, Techniques and Applications*," 2012.

[10] H. Wu, M. Ravan, and R. K. Amineh, "Holographic near-field microwave imaging with Antenna arrays in a cylindrical setup," *IEEE Trans. Microw. Theory Tech*., vol. 69, no. 1, pp. 418–430, 2021. https://doi.org/10.1109/TMTT.2020.3031897

[11] L. Wang, "Multi-frequency holographic microwave imaging for breast lesion detection," *IEEE Access*, vol. 7, 2019. https://doi.org/10.1109/ACCESS.2019.2924334

[12] L. Wang, "Enhanced holographic microwave imaging for MNP target tumor detection," *IEEE Access*, vol. 7, 2019. https://doi.org/10.1109/ACCESS.2019.2905005

[13] L. Guo and A. M. Abbosh, "Optimization-based confocal microwave imaging in medical applications," *IEEE Trans. Antennas Propag*., vol. 63, no. 8, 2015. https://doi.org/10.1109/TAP.2015.2434394

[14] W. Shao, A. Edalati, T. R. McCollough, and W. J. McCollough, "A phase confocal method for near-field microwave imaging," *IEEE Trans. Microw. Theory Tech*., vol. 65, no. 7, 2017. https://doi.org/10.1109/TMTT.2016.2637930

[15] S. A. S. Karamfard and B. M. Asl, "Fast delay-multiply-and-sum beamformer: Application to confocal microwave imaging," *IEEE Antennas Wirel. Propag. Lett*., vol. 19, no. 1, 2020. https://doi.org/10.1109/LAWP.2019.2951575

[16] M. D. Hossain and A. S. Mohan, "Cancer detection in highly dense breasts using coherently focused time-reversal microwave imaging," *IEEE Trans. Comput. Imaging*, vol. 3, no. 4, 2017. https://doi.org/10.1109/TCI.2017.2737947

[17] M. Yousefnia, A. Ebrahimzadeh, M. Dehmollaian, and A. Madannejad, "A time-reversal imaging system for breast screening: Theory and initial phantom results," *IEEE Trans. Biomed. Eng*., vol. 65, no. 11, 2018. https://doi.org/10.1109/TBME.2018.2807799

[18] S. Mukherjee, L. Udpa, S. Udpa, E. J. Rothwell, and Y. Deng, "A time reversal-based microwave imaging system for detection of breastTumors," *IEEE Trans. Microw. Theory Tech.*, vol. 67, no. 5, 2019. https://doi.org/10.1109/TMTT.2019.2902555

[19] Y. Song and N. K. Nikolova, "Memory-efficient method for wideband self-adjoint sensitivity analysis," *IEEE Trans. Microw. Theory Tech*., vol. 56, no. 8, 2008. https://doi.org/10.1109/TMTT.2008.927400

[20] L. Liu, A. Trehan, and N. K. Nikolova, "Near-field detection at microwave frequencies based on self-adjoint response sensitivity analysis," *Inverse Probl.,* vol. 26, no. 10, 2010. https://doi.org/10.1088/0266-5611/26/10/105001

[21] N. K. Nikolova, *"Introduction to Microwave Imaging*," 2017. https://doi.org/10.1017/9781316084267

[22] J. Sachs, S. Ley, T. Just, S. Chamaani, and M. Helbig, "Differential ultra-wideband microwave imaging: Principle application challenges," *Sensors (Switzerland),* vol. 18, no. 7, 2018. https://doi.org/10.3390/s18072136

[23] A. Vispa et al., "UWB device for breast microwave imaging: Phantom and clinical validations," *Meas. J. Int. Meas. Confed*., vol. 146, 2019. https://doi.org/10.1016/j.measurement.2019.05.109

[24] M. T. Islam, M. Z. Mahmud, S. Kibria, and M. Samsuzzaman, "A low cost and portable microwave imaging system for breast tumor detection using UWB directional Antenna array," *Scientific Reports*, vol. 9, no. 1, p. 15491. https://doi.org/10.1038/s41598-019-51620-z

[25] A. V. Oppenheim, R. W. Schafer, and J. R Buck, "*Discrete Time Signal Processing 2nd Edition*". Hoboken: Prentice-Hall, 1998.

[26] R. Sobot, "*Wireless Communication Electronics*". Boston: Springer, 2012. https://doi.org/10.1007/978-1-4614-1117-8

[27] S. Ramdani, A. P. Astyani, and Basari, "Filtered Back Projection and Simultaneous Algebraic Reconstruction Technique for Image Formation on Square-Shaped Physical Phantom Aimed at Microwave Imaging Applications," in Progress in Electromagnetics Research Symposium, 2018, vol. 2018-August. https://doi.org/10.23919/PIERS.2018.8597887

[28] D. Elevani, R. Ramadhan, D. T. Parastika, and Basari, "Evaluation of algebraic reconstruction technique algorithm for microwave imaging," 2016. https://doi.org/10.1109/PIERS.2016.7734395

[29] Basari and R. Aprilliyani, "The effect of data acquisition configuration on simultaneous algebraic reconstruction technique algorithm for microwave imaging system," in Asia-Pacific Microwave Conference Proceedings, APMC, 2019, vol. 2018-November. https://doi.org/10.23919/APMC.2018.8617224

[30] Basari and S. Ramdani, "Evaluation on Compressive Sensing-based Image Reconstruction Method for Microwave Imaging," in Progress in Electromagnetics Research Symposium, 2019, vol. 2019-June. https://doi.org/10.1109/PIERS-Spring46901.2019.9017424

9 Authors

Basari received his Bachelor of Electrical Engineering from Universitas Indonesia in 2002, Master of Engineering and Doctor of Engineering from Chiba University, Japan in 2008 and 2011, respectively. He worked at Indosat and Telkomsel for 2 years as an engineer in the Radio Network Planning and Radio Network Operation, respectively. Currently, Dr. Basari is a Permanent Faculty Member at the Faculty of Engineering, Universitas Indonesia since 2012 and a Researcher at the Research Center for Biomedical Engineering, Universitas Indonesia since its inception in 2016. Fields of interest in research include biomedical engineering (medical devices for informatics, diagnosis, and therapy), medical imaging, MRI, artificial intelligent applications for healthcare and wireless/wearable medical systems. He has published his scientific writings in more than 150 articles in proceedings and scientific journals. He also owns 1 granted patent, 4 licensed intellectual properties (1 patent, 1 copyright, 1 circuit design and layout, and 1 industrial design), and 4 registered patents.

Basari joins several scientific communities in the field of science such as the IEEE (Institute of Electrical and Electronics Engineers), the Association of Indonesian Biomedical Engineering Program Institutions (AIPTBI), the Association of Indonesian Biomedical Engineers (PATBI), Indonesian Hospital Engineering Association (PTPI) and the Indonesian Engineers Association (PII).

Dr. Basari is the Head of the Biomedical Engineering Programs at Universitas Indonesia (Master and UG Program), Editor in Chief of the Makara Journal of Technology, Universitas Indonesia, from 2018-now; was the Head of the IEEE MTT/AP-Society Indonesia Section Chapter for 2018, 2019 and 2020,

Basari has experiences in organizing international scientific conferences include being the General Chair of the 2016 International Symposium on Biomedical Engineering (ISBE); Vice Chair of the 2018 Indonesia Japan Joint Scientific Symposium (IJJSS), Vice Chair of the 2019 Indonesia-Japan Workshop on Antennas and Wireless Technology (IJAWT), and General Chair of the 2019 IEEE Region 10 (Asia-Pacific) Humanitarian Technology Conference (R10 HTC). Basari is also a reviewer in several international conferences and journals in the fields of Engineering, Electrical Engineering and Biomedical Engineering.

Dr. Basari has received several awards such as 2010 IEEE AP-Society Japan Chapter Young Engineer Award, 2011 Best Doctoral Graduate of Chiba University-Japan, 2013 APRASC-URSI Young Scientist Award, 2015 QiR Best Paper Award, and 2020, 2021, 2022 Engineering Dean Award. (Email: basyarie@eng.ui.ac.id)

Syahrul Ramdani received the B.Eng in electrical engineering and M.Eng in Biomedical Engineering from Universitas Indonesia, Jakarta, Indonesia. He is a lecturer and researcher in Biomedical Engineering Program in the Department of Electrical Engineering Universitas Indonesia. He is currently a visiting scholar at the University of California, Berkeley, US. (Email: syahrul.ramdani@ui.ac.id).

Article submitted 2023-02-08. Resubmitted 2023-04-25. Final acceptance 2023-04-25. Final version published as submitted by the authors.